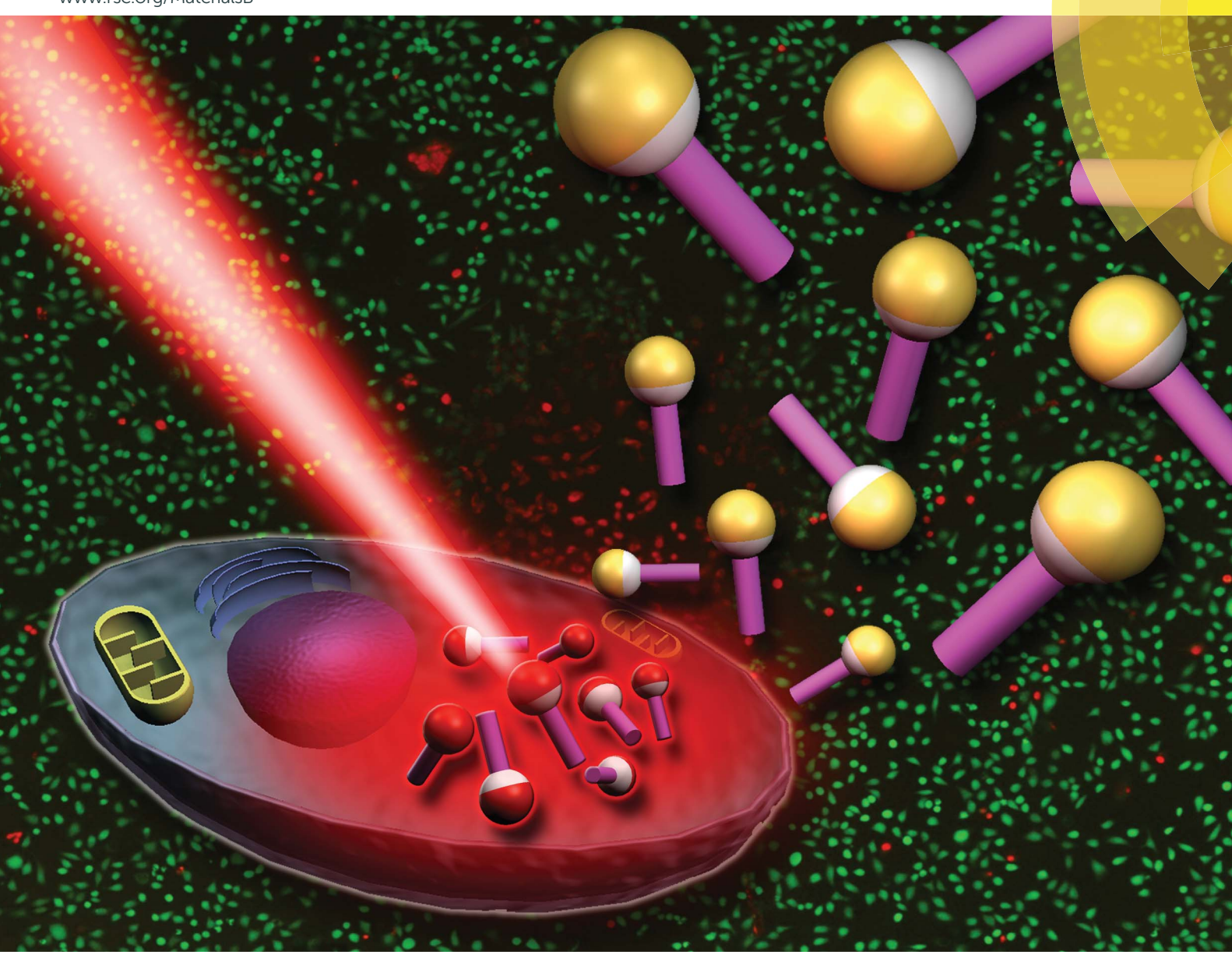
# Journal of Materials Chemistry B

Materials for biology and medicine www.rsc.org/MaterialsB



ISSN 2050-750X



## Journal of Materials Chemistry B



## COMMUNICATION

View Article Online
View Journal | View Issue



Cite this: *J. Mater. Chem. B*, 2014, **2**, 6462

Received 15th June 2014 Accepted 23rd July 2014

DOI: 10.1039/c4tb00964a

www.rsc.org/MaterialsB

## Bio-inspired nanotadpoles with component-specific functionality†

Hyelim Kang, a Shin-Hyun Kim, \*a Seung-Man Yang and Ji-Ho Park\*b

We report a new class of bio-inspired nanotadpoles (NTPs) with component-specific functionalities. The plasmonic NTPs with a gold-coated head and a reactive ion etching-treated tail showed the tail length dependence of their cellular uptake, enabling the photothermal treatment of cancer cells with high efficacy.

Natural biological materials, from pathogens to mammalian cells, are characterized by a diversity of sizes and shapes that govern their biological functions. Inspired by such materials, researchers have recently fabricated synthetic analogues with similar biological functions by mimicking the sizes and shapes of natural materials. Representative nanoscale and microscale examples include di-block copolymer micelles that resemble filamentous viruses2 and non-spherical polymeric microparticles that mimic red blood cells,3 respectively; both artificial counterparts are able to extend the blood residency time through modulation of vascular dynamics in a similar manner to natural materials. The shape of synthetic materials also plays an important role in mediating interactions with mammalian cells.4 It is known that disk-shaped particles generally show a lower tendency to be internalized into the cell compared to spherical particles when the particles have a comparable size to a virus (50-300 nm). However, the shape dependence of cellular internalization has been mostly investigated with symmetric objects such as spherical, elongated, cubic, and ellipsoidal nanoparticles.4,5

In nature, asymmetric biological structures provide unique biological functions. <sup>1a,6</sup> Biological materials with a microscale or nanoscale tadpole structure, such as human sperm cells, *Clostridium tetani* bacteria, and bacteriophages, possess distinct

head and tail regions, of which harmonious combination leads to advanced functionality. For example, the flexible tail helps the sperm swim the distance from the vagina to the fallopian tube, whereas the biodegradable head delivers the genetic materials. Bacteriophages present different biological recognition molecules on the head and tail, providing structure-dependent cellular responses. Asymmetrical synthetic materials with bifunctional structures and surface chemistries can control their biological fates in a manner that is distinct from the strategies employed by symmetric materials. Substantial efforts have been made toward developing synthetic hybrid materials that have dual-functional components for biological applications.7 Nevertheless, the unique features of asymmetrical structures are not yet fully exploited due to lack in controlled synthetic approaches.8 Therefore, a novel strategy for designing asymmetric nanoparticles and fundamental study of biological responses to these materials still remain an important challenge.

Here, we report a facile method to create bio-inspired multifunctional tadpole-like particles in a highly controlled fashion and their cellular internalization for photothermal cancer therapy. The particles are designed to have a silica head and a polystyrene tail by colloidal lithography,9 which are therefore referred to here as nanotadpoles (NTPs). The lithographic fabrication approach used here permitted the dimension of the NTPs to be adjusted in a simple manner; the tail length of the NTPs was precisely controlled to evaluate its effects on cellular uptake. These asymmetric NTPs could be further functionalized by incorporating different materials into the head and tail parts, thereby providing component-specific functionalities. The head part was either impregnated with a fluorescent dye to allow for biological imaging or was coated with a gold nano-film for plasmonic applications. The tail part was loaded with either fluorescent dyes to allow for biological imaging or with magnetic nanocrystals for magnetic separation. Plasmonic NTPs, in which the tail length was optimized for efficient cellular uptake and the gold hemisphere cap was tailored for NIR absorption, were developed to effectively destroy cancer cells based on their photothermal properties.

<sup>&</sup>lt;sup>a</sup>Department of Chemical and Biomolecular Engineering (BK21+ Program), KAIST, Daejeon, South Korea. E-mail: kim.sh@kaist.ac.kr; Fax: +82-42-350-3910; Tel: +82-42-350-3911

<sup>&</sup>lt;sup>b</sup>Department of Bio and Brain Engineering (BK21+ Program), KAIST, Daejeon, South Korea. E-mail: jihopark@kaist.ac.kr; Fax: +82-42-350-4310; Tel: +82-42-350-4330

 $<sup>\</sup>dagger$  Electronic supplementary information (ESI) available: Experimental details and figures. See DOI: 10.1039/c4tb00964a

Communication

The NTPs were fabricated using previously established colloidal lithographical methods (Fig. 1a).9b-d As the tail materials of NTPs, polystyrene (PS) films were deposited onto a polyacrylic acid (PAA)-coated silicon wafer, which were then subjected to mild O<sub>2</sub> plasma to render the surface hydrophilic; the water-soluble PAA film is used as a sacrificial layer. A hexagonally ordered single layer of monodisperse silica nanospheres (NSs) with an average diameter of 165 nm was prepared over the film by spin-casting the colloidal suspension. The assembled NSs were partially embedded onto the PS film by increasing the temperature above the glass transition temperature of PS; this promotes adhesion between silica NSs and the underlying PS film. Silica NSs on the PS film were then selectively etched out by reactive ion etching (RIE) with CF4 gas, which produces gaps between silica NSs. The nonclose-packed array of silica NSs serves as a shadow mask for the PS film under directional RIE with O2 gas; this results in the formation of hexagonally arranged tadpole-like nanostructures composed of a distinct silica head and a PS tail. The height of the tadpole-like nanostructure was controllable by varying the PS film thickness to be approximately 90, 200, and 400 nm (Fig. 1b-d); the O2 etching condition is also required to be optimized for each thickness (Table 1 in the ESI†). The tadpole-like nanostructures were then released in distilled water by dissolving the PAA sacrificial layer under ultra-sonication; the asymmetrical

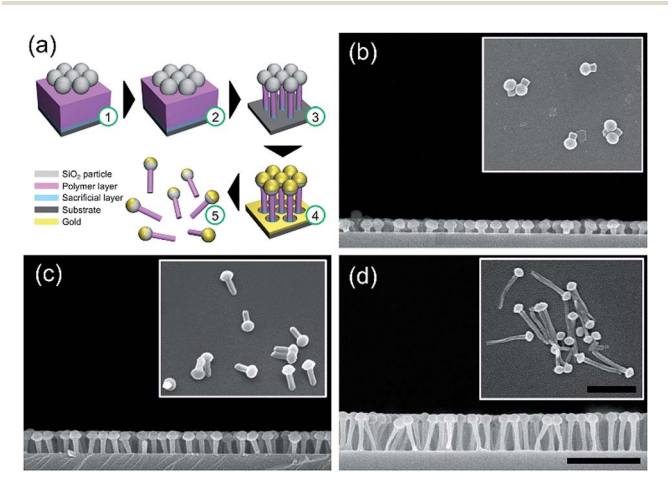


Fig. 1 Preparation of nanotadpoles (NTPs) with different tail lengths. (a) Schematic diagram illustrating the fabrication of NTPs using colloidal lithography: (1) polystyrene (PS) films were deposited onto a polyacrylic acid (PAA)-coated silicon wafer and a hexagonally ordered single layer of silica nanospheres (NSs) was prepared by using spincasting. (2) Close-packed silica NSs were embedded in the polymer layer upon heating at 110 °C for 2 min. (3) The silica NSs and polymeric layer were etched via a two-step reactive ion etching process using CF<sub>4</sub> and O<sub>2</sub> gases. (4) For plasmonic NTPs, hemispherical gold caps were deposited onto the tops of the silica heads using an e-beam evaporator. (5) Released NTPs were harvested from the substrate by ultra-sonication. (b-d) Scanning electron microscopy (SEM) images of NTPs with tail lengths of (b) 90, (c) 200, and (d) 400 nm. The inset images show the released NTPs from the substrates. The tail length of the NTP was controlled by varying the thickness of the polymeric film. Scale bars in the main panel and the inset indicate 1 µm and 500 nm, respectively.

nanostructure composed of a rigid head and a soft tail was retained during the release step (Fig. 1b-d, insets).

A variety of NTPs with distinct functionalities were prepared by incorporating different functional agents into the head and tail parts. The tail part was equipped by loading functional molecules or nanocrystals into the PS film during the spincasting step, whereas the head part was modified by either incorporating functional molecules into or depositing a metal film onto the silica NSs. For example, dual-fluorescent tadpolelike nanostructures were prepared by employing silica NSs impregnated with fluorescein isothiocyanate (FITC) onto the 9diethylamino-5-benzo[α]phenoxazinone (Nile Red)-loaded PS film. The emission spectra of an aqueous suspension of NTPs showed two distinct peaks at 525 nm and 610 nm, corresponding to FITC and Nile Red fluorescence, respectively (Fig. S1 in the ESI†). No shifts in the emission spectra were observed after the RIE process, as observed previously in the context of the fabrication of fluorescent barcode nanorods. 8e Magnetic NTPs were prepared by incorporating monodisperse magnetic iron oxide nanocrystals (MIONs) with an average size of 5 nm into the PS film during the spin-casting step (Fig. 2a and b). A transmission electron microscopy (TEM) image showed that a group of MIONs were positioned in the bottom region of the PS tail because the MIONs with a relatively high density settled down in the PS film during the spin-casting step. Energy dispersive spectrometric (EDS) analysis confirmed the presence of MIONs in the tail region by detecting their Fe elements from the dark spots (Fig. S2 in the ESI†). As expected, magnetic NTPs responded to the magnetic field and migrated to the vial wall at which an external magnet was placed (Fig. 2c).

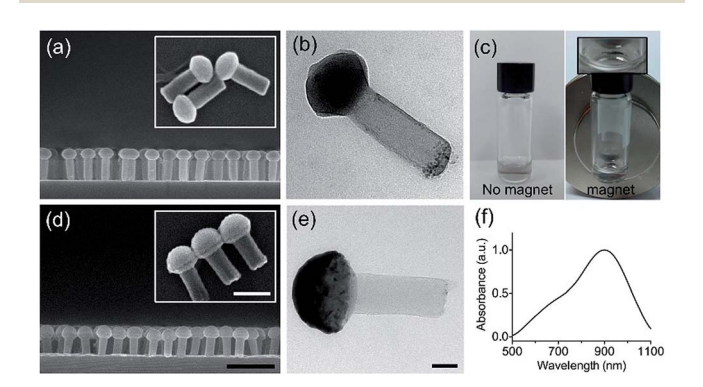


Fig. 2 Preparation and characterization of functional NTPs. (a) SEM images of magnetic NTPs with a tail length of 200 nm. Inset image shows the released magnetic NTPs from the substrates. Magnetic NTPs were prepared by incorporating iron oxide nanocrystals with an average size of 5 nm into the PS film during the deposition step. (b) Transmission electron microscopy (TEM) image of the released magnetic NTP. (c) Photographic images of the magnetic NTPs in the absence (left) or presence of an external magnetic field (right). The magnified image in the inset shows the concentrated magnetic NTPs near a magnet. (d) SEM images of plasmonic NTPs prepared with a gold film of 40 nm thickness. The gold hemisphere cap was formed on the silica NSs (head part) by depositing the gold film before the release step. (e) TEM image of the released plasmonic NTP. (f) Absorption spectrum of the aqueous suspension of plasmonic NTPs with a gold film of 40 nm thickness. The scale bars indicate 100 nm in the inset, 1 μm in the SEM images, and 50 nm in the TEM images.

Plasmonic NTPs were prepared by functionalizing the silica head part with a gold hemisphere cap. The vertical e-beam evaporation of gold onto the hexagonally arranged tadpole-like nanostructures resulted in the deposition of a hemispherical gold film coating onto the silica head (Fig. 2d and e). The EDS maps confirmed the presence of a gold hemisphere cap on the silica head (Fig. S3 in the ESI†). The gold film was not deposited onto the tail part of tadpole-like nanostructures with lengths of 90 and 200 nm because they were vertically aligned and completely shaded by the upper silica NSs during e-beam evaporation.9d By contrast, the 400 nm polymeric tail was slightly bent during the dry etching step (as shown in Fig. 1d), which resulted in the partial deposition of a gold film onto the side wall of the long tail (Fig. S4 in the ESI†). The surface plasmon resonance (SPR) properties were tuned by controlling the thickness of the deposited gold film (Fig. S5 in the ESI†). As the thickness of the gold hemisphere cap increased from 20 to 40 nm, the spectrum shifted to shorter wavelengths, from 1022 to 900 nm, as observed previously with gold nanoshells;10 the thickness of the gold film indicates thickness on the top of silica NSs. The plasmonic NTPs with a SPR peak of 900 nm were selected for subsequent biological experiments because they could be activated for photothermal therapy with non-phototoxic and tissue-penetrating near-infrared (NIR) light.11

The shape and surface chemistry of synthetic nanomaterials played important roles in mediating their interactions with mammalian cells. To investigate the influence of tail length of NTPs on cellular uptake, we used plasmonic NTPs with two different tail lengths of 90 and 200 nm and plasmonic NSs without a tail (Fig. S6 in the ESI†); plasmonic NSs are simply prepared by depositing gold onto silica NSs in the absence of the PS film. For all three particles, gold is deposited to have a thickness of 40 nm and therefore a SPR wavelength of 900 nm. The plasmonic NTPs are amphiphilic due to the significant contrast of surface properties between the head and tail; the gold-coated head is relatively hydrophobic, while the side wall of RIE-treated PS is relatively hydrophilic. We confirmed this by measuring contact angles of water drops deposited on gold and RIE-treated PS, respectively, which revealed 73° for the gold surface and 29° for RIE-treated PS (Fig. S7a and b in the ESI†). The plasmonic NTPs also showed hydrodynamic sizes comparable to their head diameter and tail length, indicating their good colloidal stability in a physiological solution (Fig. S8 in the ESI†). This allowed long-term incubation of NTPs with cells. The cellular uptake studies were conducted by treating HeLa cells with three types of plasmonic nanoparticles at a constant particle concentration of  $5.04 \times 10^9$  particles per mL for 4 h. The cells were then imaged using dark field microscopy after washing un-internalized nanoparticles out. The strong scattering of the gold hemisphere cap on the silica head enabled their visualizing as orange spots in dark field microscopy images (Fig. 3a-d). Direct comparison of the images indicates that the number of orange dots observed in the intracellular region increased as the tail length of the plasmonic nanoparticles increased. The confocal fluorescence microscopic images further confirmed their intracellular translocation (Fig. S9 and S10 in the ESI†). Higher cellular uptake for NTPs

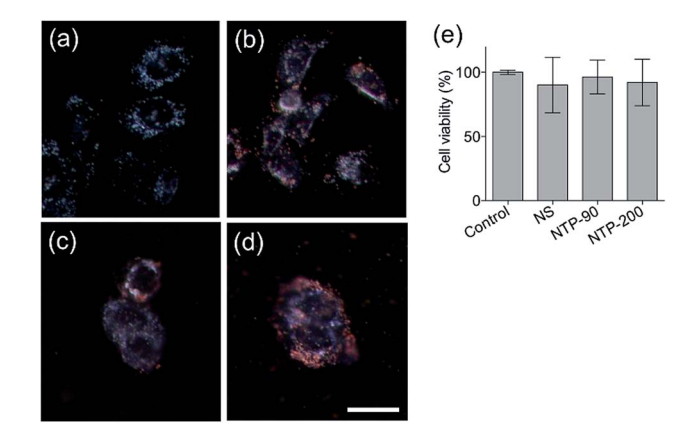


Fig. 3 Cellular response to the plasmonic NTPs and NSs. (a–d) Dark field microscopy images of HeLa cells treated with three types of plasmonic nanoparticles, where images were obtained after 4 h incubation with particles and subsequent washing of un-internalized particles: (a) no particles (control), (b) plasmonic NSs, and (c and d) two kinds of plasmonic NTPs with a tail length of (c) 90 (NTP-90), and (d) 200 nm (NTP-200). Scale bar indicates 50  $\mu$ m. (e) Cell viability analyzed using an MTT assay after additional 24 h incubation.

with a longer tail is attributed to the hydrophilicity of the tail; the hydrophilic surface strongly interacts with the plasma membrane,  $^{12}$  thereby facilitating internalization of long-tailed NTPs into the cells. The intracellular uptake could be further enhanced by synergistically tuning the part-specific surface chemistry of the NTPs.  $^{7e,13}$  The cytotoxicity of the plasmonic nanoparticles was investigated using a 3-(4,5-dimethylthiazol-2-yl)-2,5-diphenyltetrazolium bromide (MTT) assay. For this, HeLa cells were treated with three different plasmonic nanoparticles at a constant particle concentration of 5.04  $\times$   $10^9$  particles per mL for 4 h and then incubated for an additional 24 h. No significant cytotoxicity was observed in the test period for all three samples (Fig. 3e).

Finally, we tested the potential utility of the plasmonic NTPs for NIR photothermal ablation of cancer cells. The enhanced cellular uptake and strong NIR absorption of these particles were expected to lead to cancer cell death as a result of intracellular photothermal heating. Prior to the cell test, the photothermal capabilities of the particles were evaluated in bulk aqueous suspensions. The plasmonic NTPs with a tail length of 200 nm were dispersed in distilled water and then irradiated with an 808 nm laser at 450 mW for 20 min. The temperature change of the plasmonic NTP suspension was monitored in real time using a digital thermometer. As expected, the temperature gradually increased as the irradiation time increased, reaching a plateau after approximately 15 min (Fig. 4a). The temperature increase upon NIR irradiation depended on the particle concentration. The temperature of the plasmonic NTP suspension at a concentration of  $5.6 \times 10^9$  particles per mL increased by 23.7 °C, whereas the temperature of a  $1.4 \times 10^9$  particles per mL suspension increased by 17.8 °C. As a reference, the temperature of distilled water was monitored, which increased by only 5.9 °C. We next utilized the plasmonic NTPs to destroy cancer cells in vitro upon photothermal heating. HeLa cells were

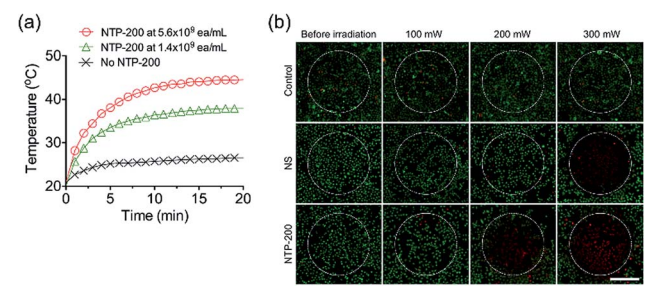


Fig. 4 Photothermal ablation of cancer cells with plasmonic NSs and NTPs. (a) Time-dependent temperature of the aqueous suspension of plasmonic NTPs with a tail length of 200 nm (NTP-200) by irradiation of an 808 nm laser with a power of 450 mW. (b) Sets of fluorescence microscopy images showing the laser irradiation-dependent viability of HeLa cells treated with no particle (control), plasmonic NS, and plasmonic NTP-200; an 808 nm laser is irradiated on the dotted circles with three distinct powers of 100, 200, and 300 mW for 1 min. The cell viability was observed using a LIVE/DEAD assay (green: live cells and red: dead cells). The scale bar indicates 500  $\mu m$ 

treated with two different plasmonic nanoparticles - plasmonic NSs and plasmonic NTPs with a tail length of 200 nm - at a constant concentration of 5.6  $\times$  10<sup>9</sup> particles per mL for 4 h and un-internalized nanoparticles were then washed out. The cells were exposed to a focused 808 nm laser beam for 1 min at three distinct powers of 100, 200, and 300 mW. The irradiated cells were then stained using a LIVE/DEAD assay to evaluate localized photohyperthermic effects of intracellularly delivered plasmonic nanoparticles. The plasmonic NTPs with a tail length of 200 nm exhibited phototherapeutic effects on the cells at a lower laser power compared to the plasmonic NSs; a power of 200 mW is sufficient to cause cell death for NTPs with a tail length of 200 nm, whereas the same power is insufficient for plasmonic NSs (Fig. 4b). Because the photothermal conversion occurred only in the presence of the metallic nanostructure, regardless of the polymer geometry, the enhanced cellular uptake of the plasmonic NTPs most likely accounted for their higher phototherapeutic outcome compared to the plasmonic NSs. Laser irradiation did not influence the cellular viability within the laser power range used. These results suggested that the amphiphilicity of the plasmonic NTPs promoted their cellular interactions and provided concomitant photothermal therapy with high efficacy.

#### Conclusions

In conclusion, we introduced a new class of bio-inspired NTPs with component-specific functionalities and enhanced cellular uptake. The tadpole-like shape bearing distinct head and tail regions was inspired by many asymmetrical biological materials, including human sperm cells, Clostridium tetani bacteria, and bacteriophages. The NTPs composed of a silica NS head and a length-tunable PS cylindrical tail were fabricated using colloidal lithographic methods. Functional NTPs were also prepared by incorporating different functional agents into the distinct head and tail components. The plasmonic NTPs with the gold-coated head and RIE-treated tail appeared amphiphilic

and showed the tail length dependence of their cellular uptake. Once they had been introduced intracellularly, the plasmonic NTPs with gold hemisphere caps effectively killed cancer cells through their NIR photothermal properties upon illumination with NIR light. The pharmacokinetic properties in vivo may be further optimized by tuning the length, surface chemistry, and flexibility of the tail component.2 The bio-inspired NTPs reported here, which exhibited shape-dependent cellular responses, are potentially useful for a wide range of biological applications.

## Acknowledgements

This work was supported by the Creative Research Initiative Program of the Ministry of Education, Science and Technology for "Complementary Hybridization of Optical and Fluidic Devices for Integrated Optofluidic Systems", the Converging Research Center Program funded by the Ministry of Science, ICT and Future Planning (Grant No. 2013K000273), and the National R&D Program for Cancer Control of the Ministry for Health and Welfare (grant no. 1220070), Republic of Korea. The authors also appreciated partial support from the KAIST High Risk High Return Project (HRHRP). We thank Heegon Kim for assistance with confocal laser scanning microscopy. Professor Yang passed away unexpectedly on September 26, 2013. This work is dedicated to his memory.

### Notes and references

- 1 (a) S. Mitragotri and J. Lahann, Nat. Mater., 2009, 8, 15; (b) J.-W. Yoo, D. J. Irvine, D. E. Discher and S. Mitragotri, Nat. Rev. Drug Discovery, 2011, 10, 521.
- 2 Y. Geng, P. Dalhaimer, S. Cai, R. Tsai, M. Tewari, T. Minko and D. E. Discher, Nat. Nanotechnol., 2007, 2, 249.
- 3 (a) N. Doshi, A. S. Zahr, S. Bhaskar, J. Lahann and S. Mitragotri, Proc. Natl. Acad. Sci. U. S. A., 2009, 106, 21495; (b) T. J. Merkel, S. W. Jones, K. P. Herlihy, F. R. Kersey, A. R. Shields, M. Napier, J. C. Luft, H. Wu, W. C. Zamboni, A. Z. Wang, J. E. Bear and J. M. DeSimone, Proc. Natl. Acad. Sci. U. S. A., 2011, 108, 586.
- 4 (a) B. D. Chithrani, A. A. Ghazani and W. C. W. Chan, Nano Lett., 2006, 6, 662; (b) J. A. Champion and S. Mitragotri, Proc. Natl. Acad. Sci. U. S. A., 2006, 103, 4930; (c) S. E. A. Gratton, P. A. Ropp, P. D. Pohlhaus, J. C. Luft, V. J. Madden, M. E. Napier and J. M. DeSimone, Proc. Natl. Acad. Sci. U. S. A., 2008, 105, 11613; (d) S. Barua, J.-W. Yoo, P. Kolhar, A. Wakankar, Y. R. Gokarn and S. Mitragotri, Proc. Natl. Acad. Sci. U. S. A., 2013, 110, 3270.
- 5 J. A. Champion, Y. K. Katare and S. Mitragotri, Proc. Natl. Acad. Sci. U. S. A., 2007, 104, 11901.
- 6 M. S. Bretcher, Nature, 1972, 236, 11.
- 7 (a) A. K. Salem, P. C. Searson and K. W. Leong, *Nat. Mater.*, 2003, 2, 668; (b) L. Y. Wu, B. M. Ross, S. Hong and L. P. Lee, Small, 2010, 6, 503; (c) G. A. Sotiriou, A. M. Hirt, P.-Y. Lozach, A. Teleki, F. Krumeich and S. E. Pratsinis, Chem. Mater., 2011, 23, 1985; (d) M. J. Sailor and J.-H. Park,

- *Adv. Mater.*, 2012, **24**, 3779; (*e*) B. Wu, S. Tang, M. Chen and N. Zheng, *Chem. Commun.*, 2014, **50**, 174.
- 8 (a) J. Hu, Y. Zhang, B. Liu, J. Liu, H. Zhou, Y. Xu, Y. Jiang, Z. Yang and Z.-Q. Tian, J. Am. Chem. Soc., 2004, 126, 9470; (b) P. H. C. Camargo, Y. Xiong, L. Ji, J. M. Zuo and Y. Xia, J. Am. Chem. Soc., 2007, 129, 15452; (c) B. Jia and L. Gao, J. Phys. Chem. B, 2007, 111, 5337; (d) X. Teng, W. Han, Q. Wang, L. Li, A. I. Frenkel and J. C. Yang, J. Phys. Chem. C, 2008, 112, 14696; (e) X. A. Li, T. Q. Wang, J. H. Zhang, D. F. Zhu, X. Zhang, Y. Ning, H. Zhang and B. Yang, ACS Nano, 2010, 4, 4350; (f) B. Liu, J. Liu, F. Liang, Q. Wang, C. Zhang, X. Qu, J. Li, D. Qiu and Z. Yang, Macromolecules, 2012, 45, 5176.
- 9 (a) S. M. Yang, S. G. Jang, D. G. Choi, S. Kim and H. K. Yu, *Small*, 2006, 2, 458; (b) S. G. Jang, H. K. Yu, D. G. Choi and

- S. M. Yang, *Chem. Mater.*, 2006, **18**, 6103; (*c*) C. J. Heo, S. H. Kim, S. G. Jang, S. Y. Lee and S. M. Yang, *Adv. Mater.*, 2009, **21**, 1726; (*d*) C.-J. Heo, H. C. Jeon, S. Y. Lee, S. G. Jang, S. Cho, Y. Choi and S.-M. Yang, *J. Mater. Chem.*, 2012, 22, 13903; (*e*) H. Kang, C. J. Heo, H. C. Jeon, S. Y. Lee and S. M. Yang, *ACS Appl. Mater. Interfaces*, 2013, **5**, 4569.
- 10 S. J. Oldenburg, R. D. Averitt, S. L. Westcott and N. J. Halas, Chem. Phys. Lett., 1998, 288, 243.
- 11 R. Weissleder, Nat. Biotechnol., 2001, 19, 316.
- 12 A. Verma and F. Stellacci, Small, 2010, 6, 12.
- (a) A. Verma, O. Uzun, Y. Hu, Y. Hu, H.-S. Han, N. Watson,
   S. Chen, D. J. Irvine and F. Stellacci, *Nat. Mater.*, 2008, 7,
   (b) R. C. Van Lehn, P. U. Atukorale, R. P. Carney,
   Y.-S. Yang, F. Stellacci, D. J. Irvine and A. Alexander-Katz,
   Nano Lett., 2013, 13, 4060.